A Portable Wideband CMOS NMR Spectrometer for Multinuclear Molecular Fingerprinting

Aoyang Zhang, *Member, IEEE*, Daniel Krüger, *Member, IEEE*, Behdad Aghelnejad, Guang Yang, Henry Hinton, *Member, IEEE*, Yi-Qiao Song, and Donhee Ham, *Fellow, IEEE*

***Abstract*— We present a small wideband CMOS nuclear magnetic resonance (NMR) spectrometer capable of multinuclear molecular fingerprinting (molecular structure determination). The spectrometer combines a small permanent magnet and a wideband digitally assisted CMOS radio frequency (RF) transceiver integrated circuit (IC) that operates in the RF frequency range from 1 to 100 MHz. This small, thus broadly deployable, NMR system can find applications in online, on-site, or on-demand multinuclear molecular fingerprinting. Concretely, the wideband spectrometer performs NMR spectroscopy with nuclear spins from ^{1}H, ^{19}F, and ^{2}H with a spectral resolution down to 0.07 ppm to determine structures of molecules containing these nuclear spins; it can also perform NMR with the nuclear overhauser effect (NOE), which is an important modality that further enhances the capability for molecular fingerprinting (we demonstrate the NOE by reading the ^{19}F NMR signal that is enhanced via heteronuclear magnetization transfer from ^{1}H spins). The wideband operation of the CMOS RF transceiver IC is made possible by integrating a delay-locked loop (DLL) with a broad locking range. The RF receiver (RX) part of the IC achieves an input-referred noise less than 1.2 nV/$\sqrt{\text{Hz}}$ across the entire bandwidth of 1–100 MHz, while the RF transmitter (TX) part employs a digital power amplifier.**

***Index Terms*— Application-specific integrated circuit (ASIC), CMOS, nuclear magnetic resonance (NMR), nuclear overhauser effect (NOE), radio frequency (RF) transceiver.**

I. Introduction

NUCLEAR magnetic resonance (NMR) can determine molecular structures at atomic resolution and, thus, serves as an important tool in organic, bio, and medicinal chemistry, and in structural biology [1], [2], [3]. Conventional NMR systems based on large superconducting magnets with a strong static magnetic field (B_0) are essential in determining the structures of large molecules, such as proteins, which represents a frontier NMR research. At the same time, identifying—-or fingerprinting—-small molecules via their NMR-based structural determination, which also holds great importance in chemistry and biology, can be done with a weak B_0 field that can be produced by a small (thus portable) permanent magnet.

Over the past 15 years, a number of small NMR systems have been developed by combining such small permanent magnets with CMOS radio frequency (RF) transceiver integrated circuits (ICs) [4], [5], [6], [7], [8], [9], [10], [11], [12], [13], [14], [15], [16]. Here, the RF transceivers designed to work at around the resonant frequency $f_0 = \gamma B_0/(2\pi)$ of nuclear spins of interest (also known as Larmor precession frequency, where γ is the gyromagnetic ratio of the nuclear spin) play the critical role of exciting the nuclear spins and reading out their precession motions. Such small NMR systems can be broadly deployed beyond dedicated facilities for on-site small-molecule fingerprinting.

NMR experiments may be categorized into relaxometry and spectroscopy. Relaxometry measures relaxation dynamics of a collection of excited nuclear spins. Concretely, an ensemble of nuclear spins that exhibit precession motions about the B_0 field will gradually lose phase coherence in their precession motions due to spin–spin interactions, and consequently, the measured sinusoid due to the ensemble precession will be damped with a characteristic relaxation time known as T_2. Relaxometry, which measures T_2, is valuable for interrogating materials, because T_2 varies with material compositions. But, molecular fingerprinting requires spectroscopy—-which is more demanding than relaxometry—-to determine molecular structure. Let an organic molecule containing a number of ^{1}H atoms be subjected to B_0. Since the molecule itself generates small local static magnetic fields, which can add onto or subtract from B_0, ^{1}H proton spins at different locations in the molecule can exhibit different resonant frequencies slightly deviated from $f_0 = \gamma B_0/(2\pi)$. Thus, spectroscopy—-i.e., measurement of these finely shifted frequencies—-can be used to determine the structure of the molecule and, hence, is essential for molecular fingerprinting. Spectroscopy is more difficult than relaxometry due to the higher field homogeneity required for B_0 (and a system capable of spectroscopy is always capable of relaxometry), but by now, many of the miniaturized NMR

Manuscript received 1 September 2023; revised 14 December 2023 and 23 January 2024; accepted 24 January 2024. Date of publication 15 July 2024; date of current version 26 September 2024. This article was approved by Associate Editor Ron Kapusta. This work was supported by the Advanced Research Projects Agency-Energy (ARPA-E; Program Directors, Dr. Isik Kizilyalli and Dr. Olga Spahn) under Contract DE-AR0001063. *(Corresponding author: Donhee Ham.)*

Aoyang Zhang was with Harvard John A. Paulson School of Engineering and Applied Sciences, Harvard University, Cambridge, MA 02138 USA. He is now with the School of Integrated Circuits, Tsinghua University, Beijing 100084, China.

Daniel Krüger, Guang Yang, Henry Hinton, Yi-Qiao Song, and Donhee Ham are with Harvard John A. Paulson School of Engineering and Applied Sciences, Harvard University, Cambridge, MA 02138 USA (e-mail: donhee@seas.harvard.edu).

Behdad Aghelnejad was with Harvard John A. Paulson School of Engineering and Applied Sciences, Harvard University, Cambridge, MA 02138 USA. He is now with Oxford Instruments, OX13 5QX Abingdon, U.K.

Color versions of one or more figures in this article are available at https://doi.org/10.1109/JSSC.2024.3362808.

Digital Object Identifier 10.1109/JSSC.2024.3362808

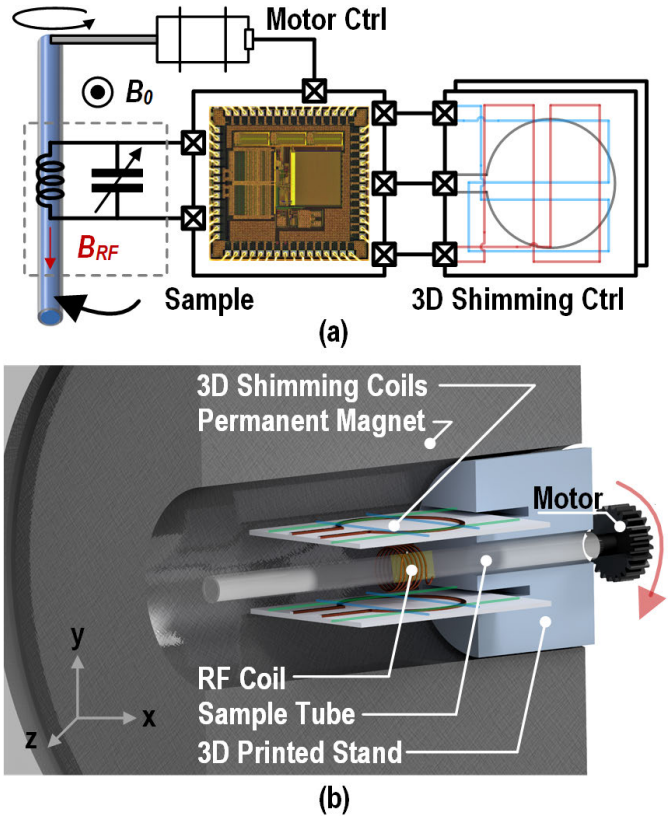

Fig. 1. (a) Illustration of our small wideband CMOS NMR spectrometer. (b) Illustration of the magnet bore inside the NMR system.

systems have achieved spectroscopy [6], [7], [10], [12], [13], [15], [16].

In this article, which is an extended version of our earlier conference paper [17], we present a small NMR spectroscopy system combining a Halbach permanent magnet (B_0 ~0.51 T) with a wideband (1–100 MHz) CMOS RF transceiver IC. The wideband transceiver allows for performing NMR not only with the most common ^{1}H proton spins (f_0 ~21.8 MHz) but also with other nuclear spins, such as ^{19}F (f_0 ~20.5 MHz) and ^{2}H (f_0 ~3.3 MHz), and this ability to handle different types of NMR active nuclei expands the molecular fingerprinting capability of miniaturized NMR. Furthermore, the wideband transceiver allows for performing the nuclear overhauser effect (NOE) experiment, where an NMR signal for one type of nuclear spins is enhanced by another type of nuclear spins via magnetization transfer. In NMR spectroscopy, the NOE provides another window on examining molecular structures and interactions.

Section II provides an overview of our NMR system. Section III describes the design of the CMOS RF transceiver IC. Section IV presents the characterization of the IC and NMR experiments. Section V provides the conclusion.

II. System Overview

Fig. 1 schematically illustrates our small NMR system. Its two main components are the Halbach permanent magnet (B_0 ~0.51 T; weight: 7.3 kg and size: 12 × 11.5 × 12.5 cm) and the wideband CMOS RF transceiver IC. A sample-containing tube wound with an RF coil is placed in the magnet bore, and the RF coil is connected to the CMOS RF transceiver IC. The intrinsic B_0 field inhomogeneity of the permanent magnet near the center of its bore is ~0.4 ppm across a 0.15-μL volume along a length of 1.2 mm and a cross-sectional area of 0.126 mm^2. To resolve fine NMR spectra, such as J coupling, a B_0 field inhomogeneity less than 0.1 ppm is desired. To achieve this level, we add shimming coils implemented on printed circuit boards (PCBs) inside the magnet bore. To further lower the field inhomogeneity, we rotate the sample tube at 2000 revolutions per minute (rpm) or at ~33 Hz. The resulting motional averaging reduces the field inhomogeneity across the plane perpendicular to the rotation axis. This rotation combined with the shimming coils results in field inhomogeneity (and thus spectral resolution) down to 0.07 ppm.

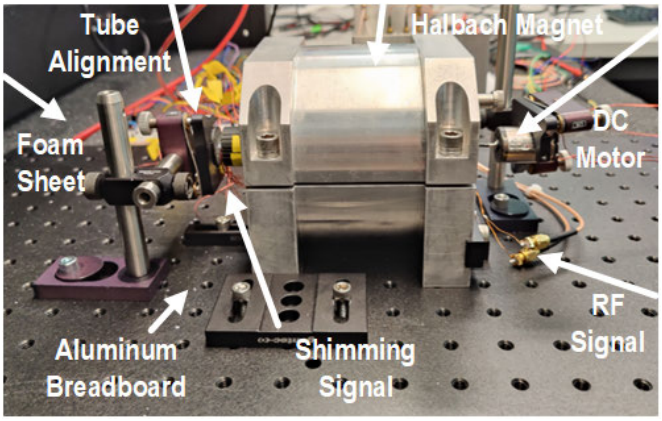

Fig. 2. Close-up view of the small NMR spectrometer system equipped with both shimming coils (view blocked by the magnet) and sample rotation capability.

Fig. 2 is a photograph of our actual NMR spectrometer equipped with both shimming coils (hidden in the magnet) and the sample rotation capability. The system is mounted on an aluminum breadboard and placed on a foam sheet to minimize mechanical perturbations, such as those from the sample rotation. An additional tube alignment plate is added to fix the sample's position during the sample rotation. Shimming and sample rotation are needed and used for spectroscopy but not for relaxometry, for relaxometry does not have a stringent B_0 field inhomogeneity requirement.

III. Circuit Implementation

A. Overall Block Diagram

The architecture of the CMOS RF transceiver IC is illustrated in Fig. 3. It includes an RF receiver (RX), an RF transmitter (TX) including a wideband delay-locked loop (DLL), three digital-to-analog converters (DACs) for 3-D shimming control, and a 64 × 89 bit memory bank to store NMR RF pulse sequence information.

B. Wideband Receiver

In the heterodyning RF RX, the voltage signal across the RF coil induced by nuclear spin precessions is first amplified by a

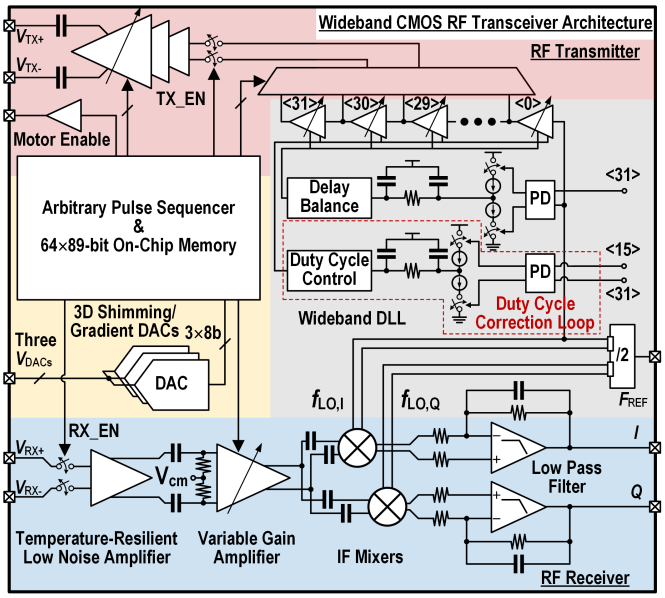

Fig. 3. CMOS RF transceiver architecture.

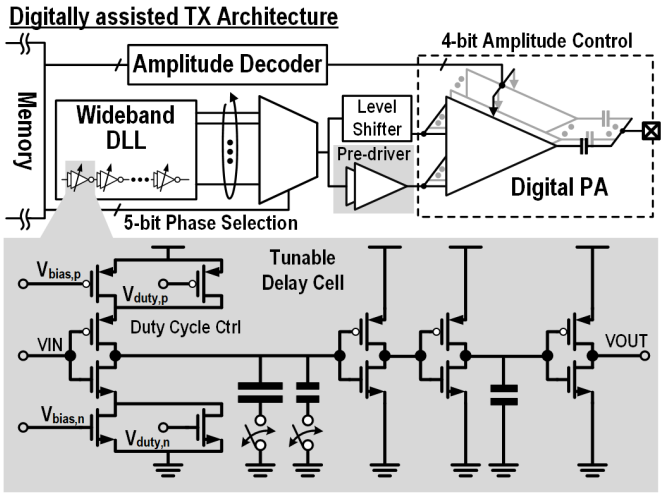

Fig. 4. Wideband TX architecture.

low-noise amplifier (LNA), followed by a variable gain amplifier (VGA), and is subsequently downconverted by quadrature mixers and further amplified by intermediate frequency (IF) amplifiers. Note that the LNA output is ac coupled with a high-pass corner frequency of 400 kHz, mitigating the dc offset, dc drift, and $1/f$ noise whose corner is smaller than 1 MHz. The LNA utilizes the same structure as in our previous work [16], but with different sizing and additional guard rings to minimize noise coupling from the substrate. The voltage gain of the RX is programmable between 30 and 110 dB. The gain of the LNA is 24 dB, and the VGA gain is tunable from -60 to 20 dB. Similar to the LNA, the VGA output is ac coupled with the high-pass corner frequency of 400 kHz. The quadrature mixer and the IF amplifier together provide an overall gain of 66 dB, where the signal is downconverted to quadrature outputs at an IF frequency (typically below 50 kHz) and low-pass filtered. For large RX gain values, an unwanted dc offset from self-mixing can cause

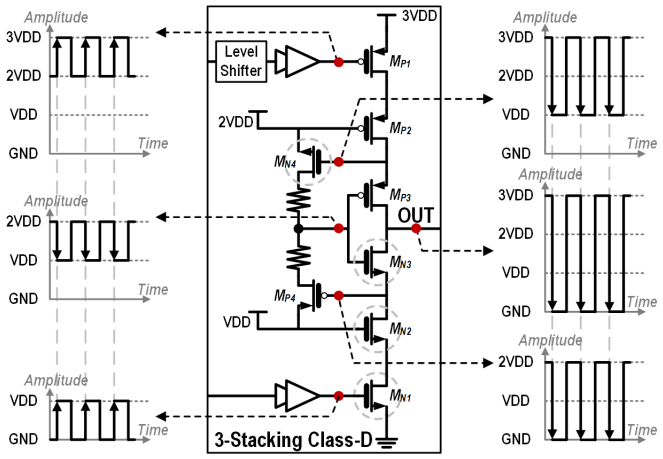

Fig. 5. Schematic of self-biasing three-stack Class-D PA.

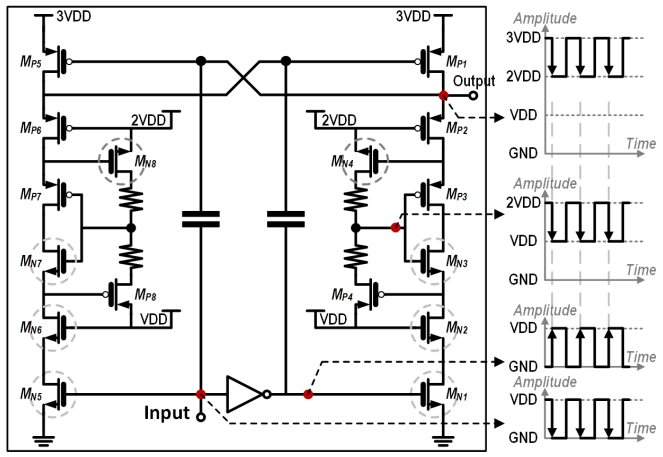

Fig. 6. Schematic of self-biasing three-stack level shifter.

RX saturation. Our design uses a passive double-balanced switching mixer with adequate linearity, suppression of spurious products, and isolation between LO and RF signals to sufficiently minimize the dc offset for our NMR work. In certain other NMR applications more vulnerable to the offset, design techniques, such as trimming, autozeroing, and dc servo loop, can be used to further suppress the offset [9], [24], [26].

C. Wideband Transmitter

The wideband TX is shown in Fig. 4. It mainly consists of a wideband DLL and a digital power amplifier (PA). The digital PA, which utilizes a switched capacitor architecture [18], consists of 15 PA unit cells. A notable characteristic is the programmable nature of these PA cells, each of which can be in an on and off mode, thus allowing for the generation of a diverse range of output power profiles.

The DLL generates 32 uniform phases and chooses any one of them for the excitation RF signal. Its 2-bit delay cells with switched capacitors are utilized to tune the delay. Compared with a narrowband DLL, even though this wideband DLL has a larger chip area and a higher power consumption because of the additional switched capacitor-based delay cells, it achieves

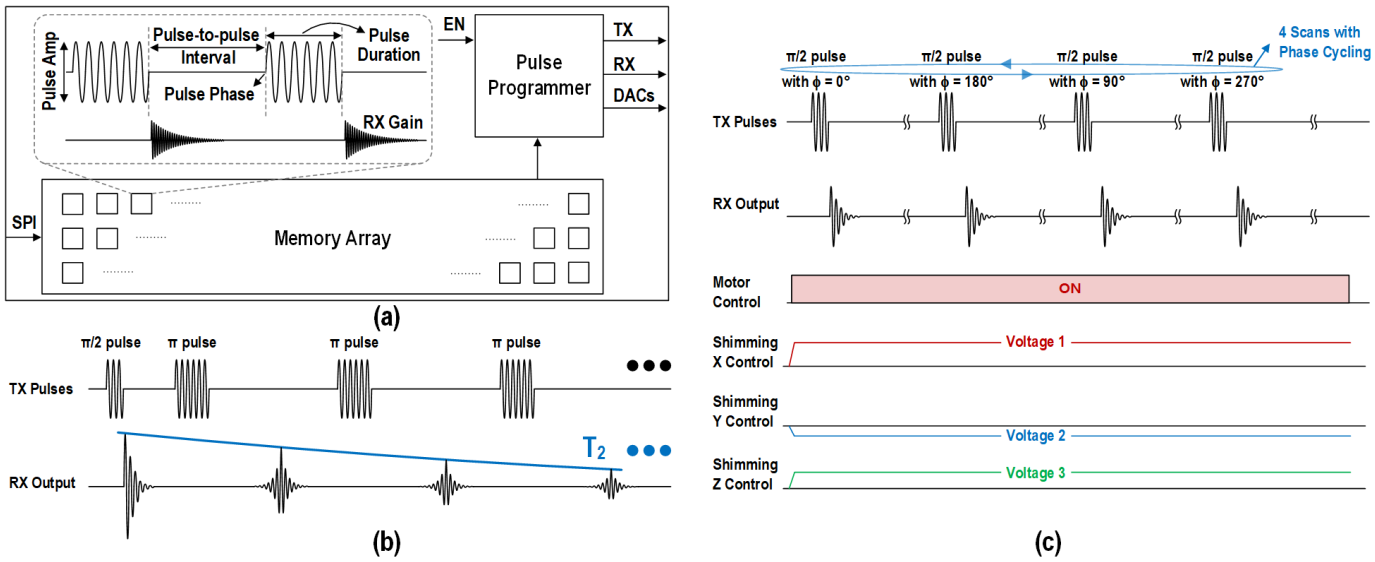

Fig. 7. (a) Memory bank and pulse programmer. (b) CPMG RF pulse excitation sequence (top) and resulting spin echoes (bottom) in the case of a large B_0 field inhomogeneity. (c) Sequence of $\pi/2$ RF excitation pulses with RF phase cycling (top) and resulting FIDs in the case of a small B_0 field inhomogeneity. The Fourier transform of any FID leads to NMR spectra. The phase cycling is to remove pulse imperfections.

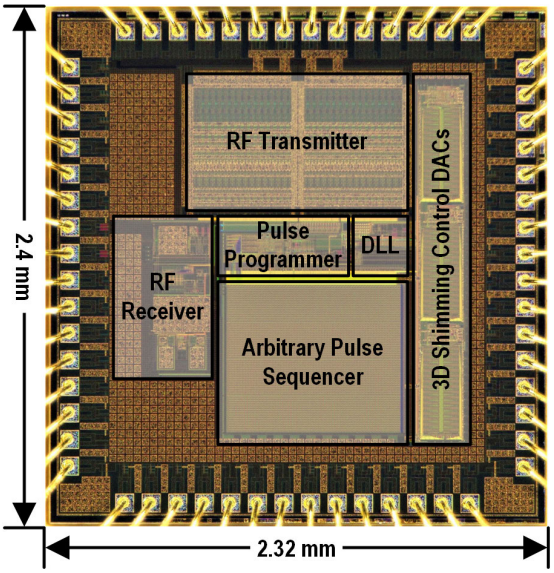

Fig. 8. Die micrograph.

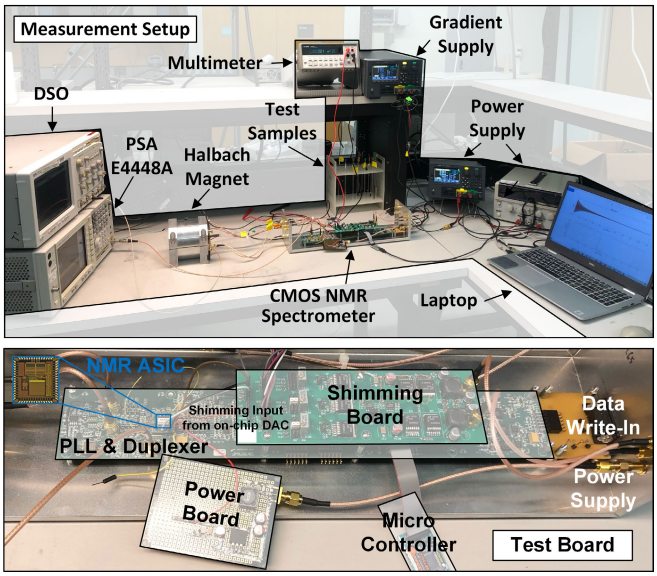

Fig. 9. Measurement setup.

a wide locking range (1–100 MHz) to operate over a wide range of frequencies. This enables the wideband operation of the CMOS RF transceiver. For the DLL, an additional duty-cycle correction loop is used to maintain a 50% duty cycle, avoiding output power degradation (see Fig. 4) [6], [7], [12], [16]. Overall, an arbitrary pulse sequencer (Section III-E) in conjunction with the DLL can produce a suite of RF excitation signals by combining 14 amplitudes, 32 phases, and various time delays. This controls the amplitude and phase of the digital PA to perform versatile manipulation of nuclear spins.

D. Self-Biasing Class-D PA (as Part of the Transmitter)

Each PA unit cell is of Class-D topology. Compared with Class-AB and Class-B PAs, the Class-D PA topology achieves better power efficiency and eliminates the need for off-chip RF chokes. However, its output voltage swing is constrained by the device breakdown voltage. To overcome this and to increase the output swing, we design a self-biasing three-stack Class-D PA (see Fig. 5). When the gate of transistor M_{N1} switches to VDD, transistors M_{N1} and M_{N2} turn on sequentially. Then, the gate of transistor M_{P4} is biased at GND, switching the gate of transistor M_{N3} to VDD. The pull-down path turns on, and the PA driver output becomes GND. Similarly, when the gate of transistor M_{P1} toggles to 2VDD, transistors M_{P1} and M_{P2} turn on, and the gate of transistor M_{N4} is biased at 3VDD, switching the gate of transistor M_{P3} to 2VDD. The pull-up path turns on, and the PA driver output becomes 3VDD. The gate voltages of transistor M_{N3} and M_{P3} dynamically change when the transistors are on and off; the output then toggles between 3VDD and GND.

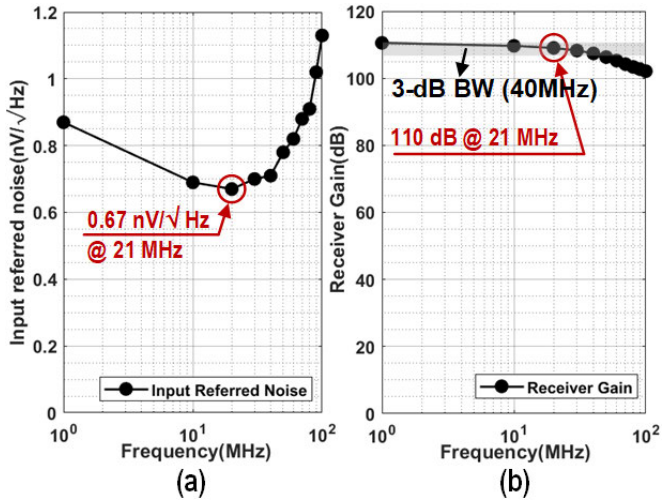

Fig. 10. (a) Measured RX input-referred noise versus frequency. (b) Measured RX gain versus frequency.

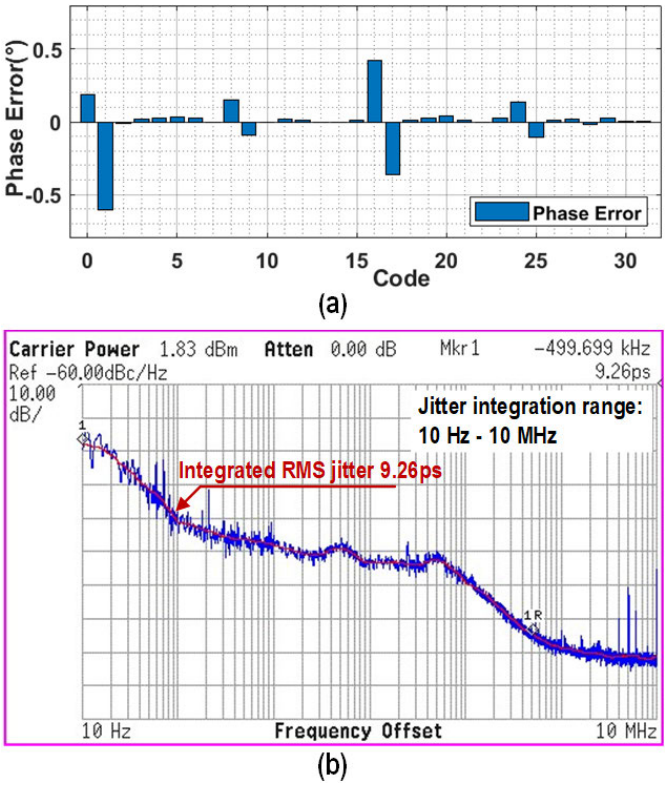

Fig. 11. (a) Measured DLL phase errors for the 32 phases. (b) Measured DLL output phase noise.

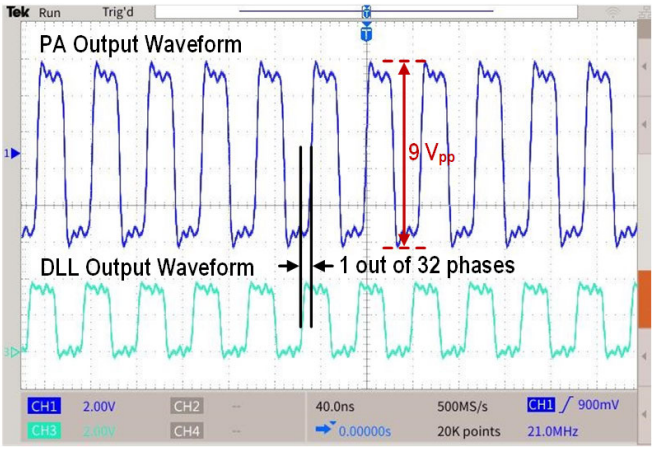

Fig. 12. Measured PA and DLL output waveforms.

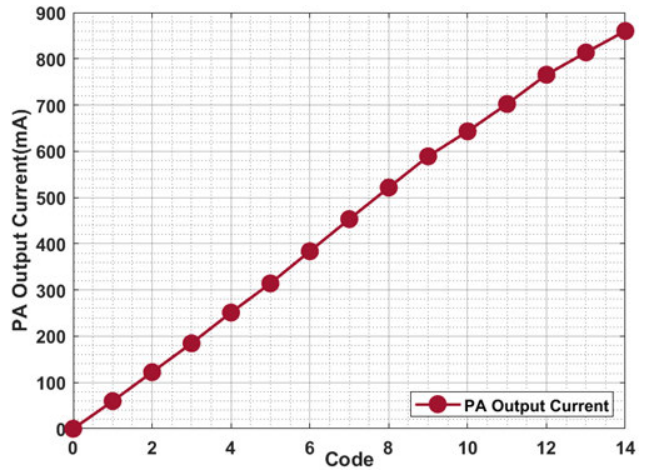

Fig. 13. Measured PA output current.

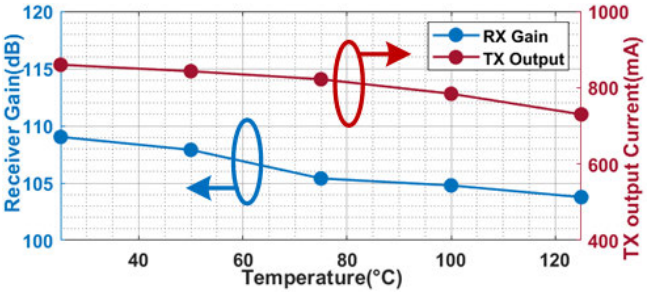

Fig. 14. Measured RX gain and TX output current versus temperature (for this temperature-varied measurement with a heat gun, we do not use the power board shown in Fig. 9 but use direct power supplies to avoid heat damage).

This self-biasing three-stack Class-D PA can alleviate the voltage stress for transistors, as compared with the conventional three-stack PA [19]. In the scheme of [19], the gate terminal of transistor M_{N3} would be connected to VDD. When the PA output (device drain node) varies from 0 to 3VDD, the gate-to-drain voltage becomes 2VDD (twice the nominal voltage), and therefore, it is subjected to voltage stress. In contrast, in the self-biasing three-stack Class-D PA, the voltage across the gate and drain is always VDD, eliminating the voltage stress and reducing the dynamic power loss caused by the gate parasitic capacitors. In addition, the self-biasing three-stack Class-D PA only needs two input signals of transistors M_{N1} and M_{P1} to switch on and off, without the need of any additional control signals [19].

Fig. 6 shows the schematic of a self-biasing three-stack level shifter. The level shifter can shift the input signal from GND/VDD to 2VDD/3VDD. The level shifter has a circuit structure similar to the PA driver, but its speed is enhanced by the addition of two capacitors.

To alleviate the voltage stress of the body terminal when the stacked devices are turned on, deep n-well (DNW) devices

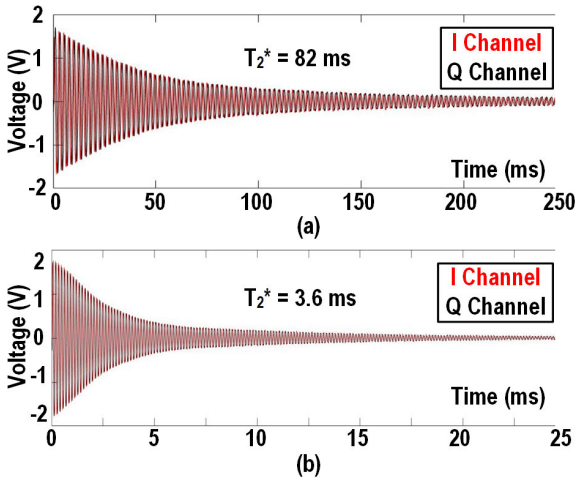

Fig. 15. ^{1}H FID (water) for with B_0 ~0.51 T and B_0 ~0.3 T with no B_0 field inhomogeneity compensation.

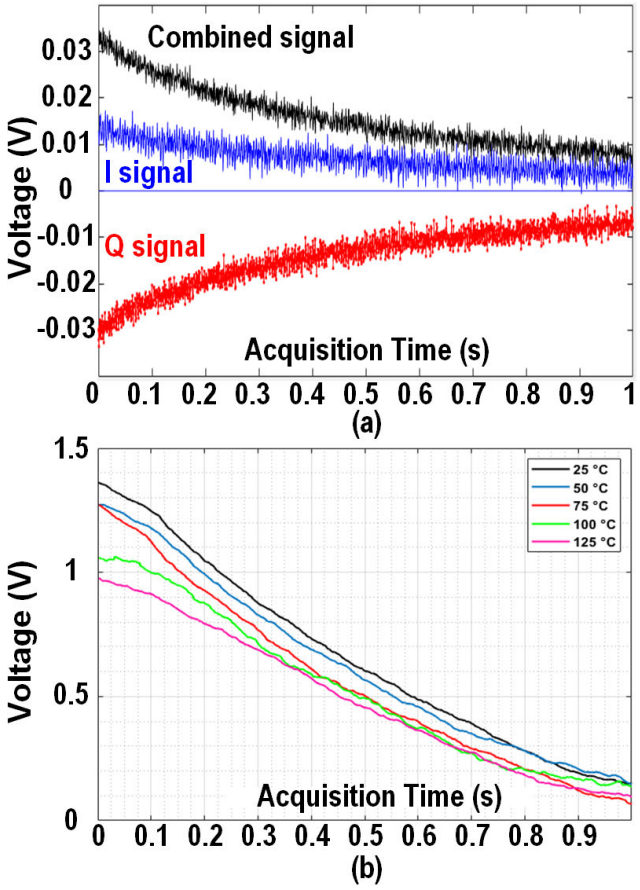

Fig. 16. (a) ^{1}H NMR relaxometry measurement with CPMG sequence (B_0 ~0.51 T, water, single scan). (b) ^{1}H NMR relaxometry measurement with CPMG sequence at different temperatures (B_0 ~0.51 T, water, each trace is a 16-scan sum).

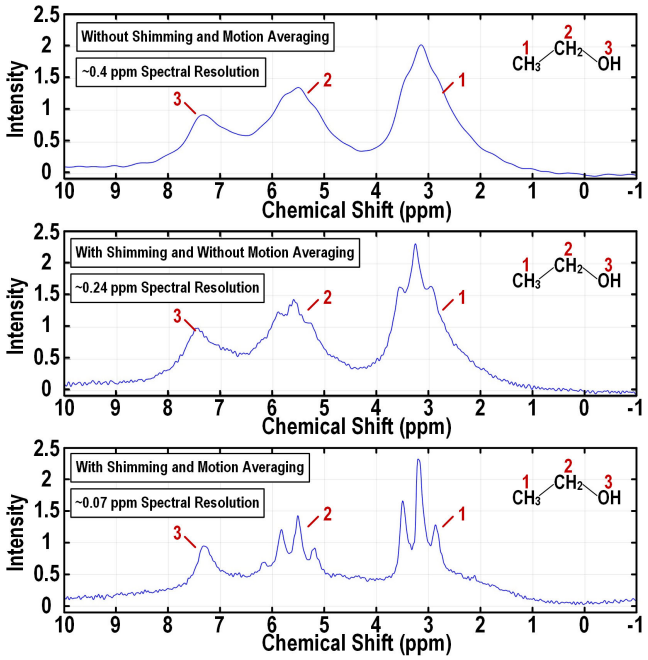

Fig. 17. Measured ethanol ^{1}H NMR spectroscopy. (a) With neither shimming nor motional averaging. (b) With shimming and without motional averaging. (c) With both shimming and motional averaging.

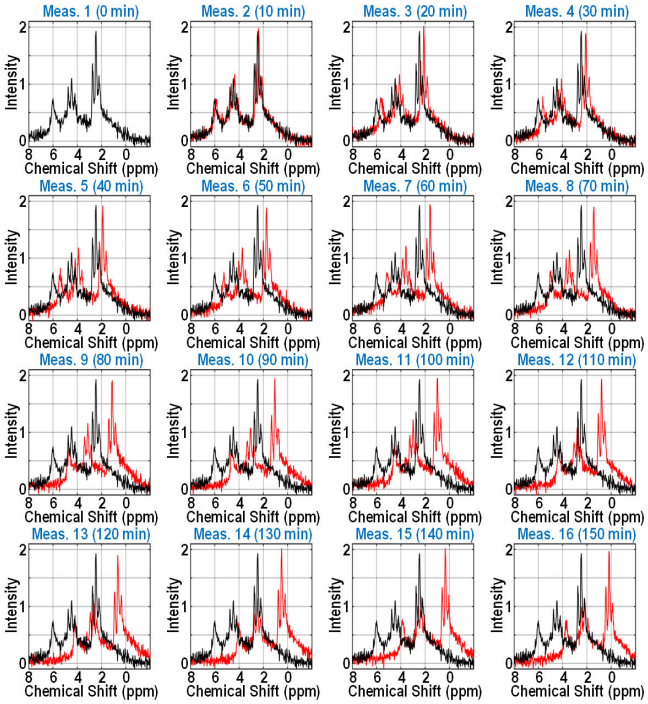

Fig. 18. Each spectrum, black or red, is an average of 16 ^{1}H NMR spectroscopy scans of ethanol, with temperature drift during the 16 scans eliminated by software method. The black 16-scan average is the first set measured and is shown repeatedly across all 16 panels. The red spectrum in the nth panel (n = 2, 3, ..., 16) is the nth 16-scan average (the time gap between the starts of any two adjacent red 16-scan averages is 10 min). The spectral shift over ca. 150 min exceeds 2 ppm.

are used to separate the nMOS transistors' bodies, so that their bodies and source terminals can be shorted together. The DNW layer is connected to 3VDD through a large isolation resistance, which avoids forward biasing and reduces the parasitic capacitance power loss associated with the diodes.

E. Memory Bank and Programming Sequence

The chip contains an on-chip 64 × 89 bit memory bank with an arbitrary pulse sequencer [see Fig. 7(a)] [12], [16]. This memory bank stores circuit configuration parameters (e.g.,

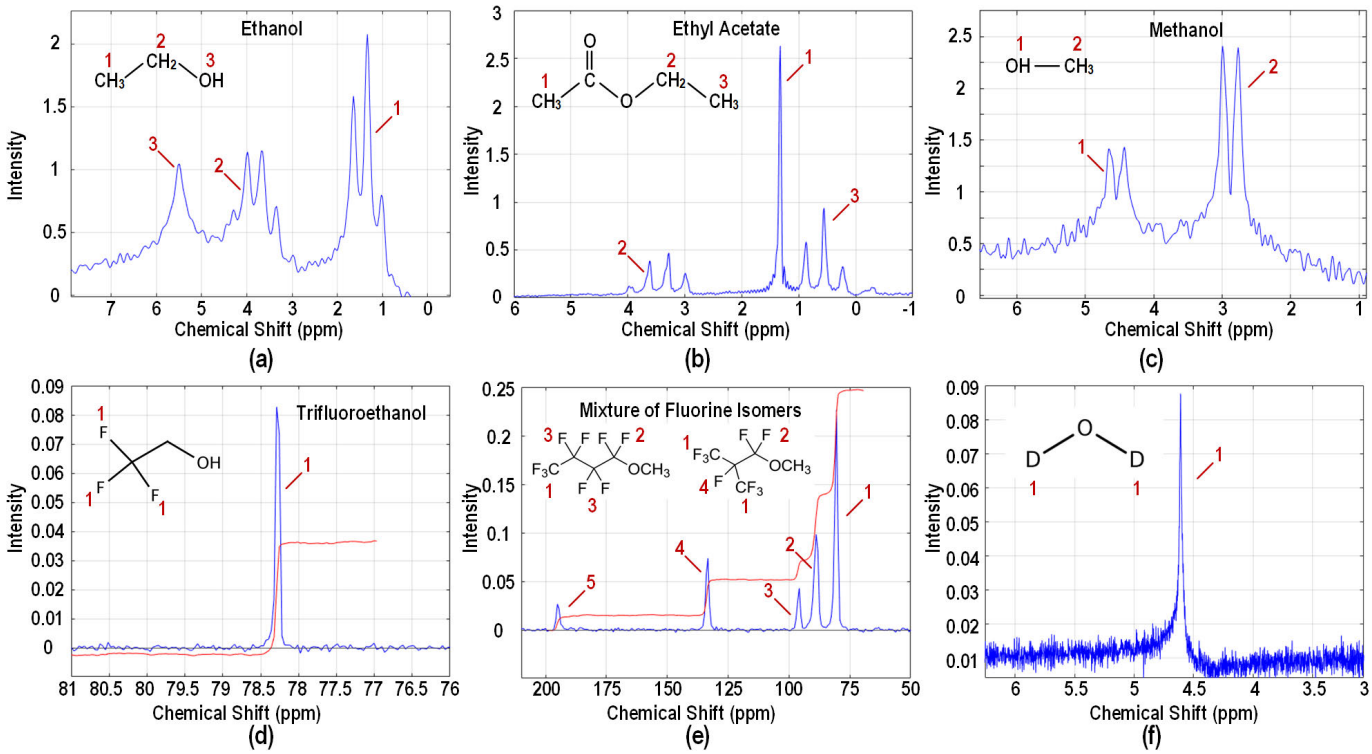

Fig. 19. Multinuclear NMR spectroscopy results. (a) ^{1}H NMR spectroscopy of ethanol. (b) ^{1}H NMR spectroscopy of ethyl acetate. (c) ^{1}H NMR spectroscopy of methanol. (d) ^{19}F NMR spectroscopy of trifluoroethanol. (e) ^{19}F NMR spectroscopy of methyl nonafluorobutyl. (f) ^{2}H NMR spectroscopy of deuterium oxide.

target RX gain and RX activation time for NMR readout), instructions for 3-D shimming control (Section III-F), and information for an NMR RF excitation pulse sequence (e.g., pulse duration, pulse amplitude, RF pulse phase, and pulse-to-pulse interval).

Fig. 7(b), top, shows an example excitation RF pulse sequence known as the Carr–Purcell–Meiboom–Gill (CPMG) sequence [20], [27], which comprises a $\pi/2$ pulse (the duration of this excitation pulse is such that it rotates a nuclear spin by $\pi/2$) followed by a train of π pulses. The CPMG sequence can be used for relaxometry in the case of a large B_0 field inhomogeneity; that is, the CPMG sequence overcomes the effect of the large B_0 field inhomogeneity to obtain T_2 due to spin–spin interactions [the resulting precession signal registered at the RX appears as what is known as spin echoes [see Fig. 7(b), bottom] and their envelop decays at T_2]. Fig. 7(c) is another example RF pulse sequence, which is a repetition of $\pi/2$ pulses, but with RF pulse phase cycling (0°, 90°, 180°, and 270°). In the case of a small B_0 field inhomogeneity, the resulting precession signal registered at the RX, after each excitation pulse, is a T_2-damped sinusoid known as the free induction decay (FID), whose Fourier transform gives the NMR spectra. The phase cycling is to remove pulse imperfections, such as pulse amplitude errors.

F. Three-Dimensional Shimming DACs

We built three 8-bit on-chip DACs for shimming control. The output voltage of each DAC is further amplified by off-chip amplifiers to drive the shimming coils. Each DAC utilizes an R–$2R$ topology and incorporates a chopper-stabilized op-amp to counter offsets and $1/f$ noise [12], [16]. The chopping frequency is set at 10 MHz to exceed the $1/f$ noise corners of the op-amp transistors and, thus, to suppress $1/f$ noise. This frequency selection also ensures that the associated 10-MHz ripples interfere neither with the RF frequency (∼21 MHz) nor with the downconverted IF frequency (typically below 50 kHz) within the transceiver.

IV. Measurement

The wideband NMR RF transceiver IC is fabricated using a 0.18-μm CMOS technology with a die size of 2.32 × 2.4 mm (see Fig. 8). The chip is packaged using a standard 60-pin QFN package. The digital memory is powered by 1.8 V, whereas the analog circuits except the PA are powered by 3.3 V. The PA is powered by 9.9 V, as described previously, i.e., 3VDD. The RX dissipates a maximum power of 47 mW. To test this transceiver, we used a microcontroller to generate the SPI control sequence. Fig. 9 shows the experimental setup of the CMOS NMR spectrometer, which contains the chip on a PCB, the 0.51-T Halbach magnet, PCBs hosting shimming coils, a dc motor, and a test sample. The oscilloscope measures the PA output waveform, while the spectrum analyzer captures DLL output phase noise.

A. Electrical Measurements

Before validating the NMR system, we first measured the CMOS RF transceiver IC. Fig. 10 shows the measured RX input-referred noise versus frequency and the measured RX

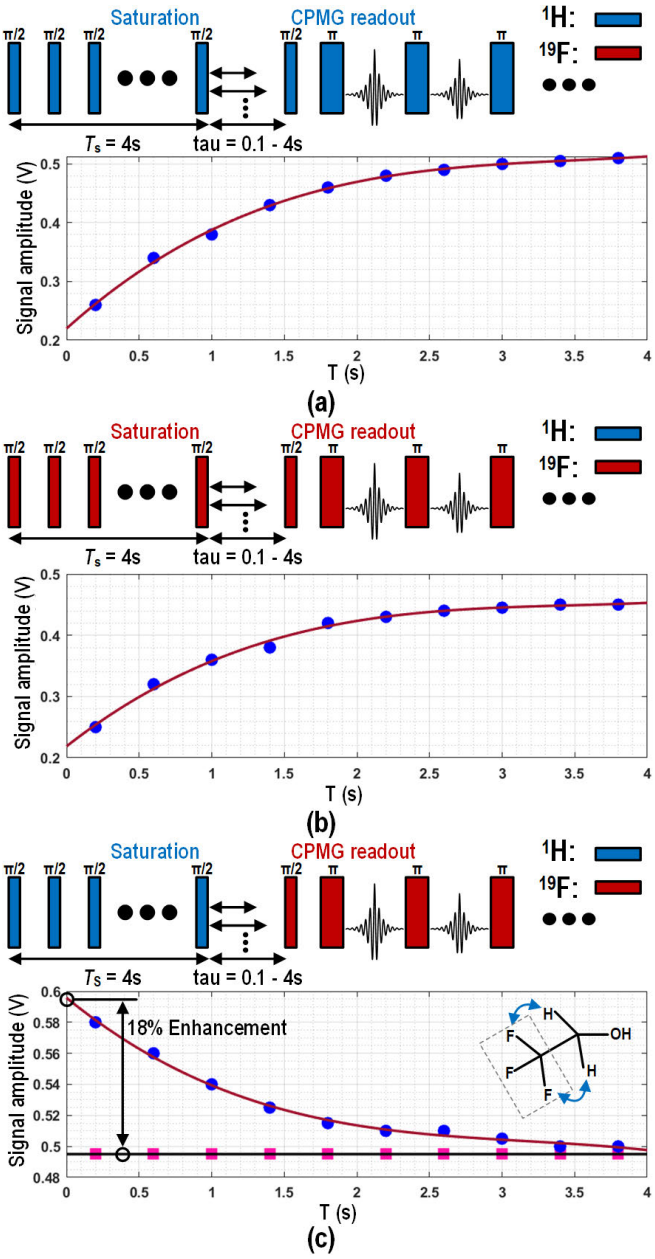

Fig. 20. (a) Measurement of ^{1}H saturation. (b) Measurement of ^{19}F saturation. (c) ^{1}H–^{19}F heteronuclear NOE measurement.

gain versus frequency. The input-referred noise is obtained by measuring the output voltage noise with the input voltage terminals shorted and then by dividing the measured output noise with the measured, maximally tuned, voltage gain. The RX input-referred noise remains below 1.2 nV/$\sqrt{}$Hz across the 1–100 MHz bandwidth, reaching 0.67 nV/$\sqrt{}$Hz at 21 MHz [see Fig. 10(a)], approximately the ^{1}H NMR frequency for B_0 = 0.51 T. The transceiver has a maximally tuned RX gain exceeding 100 dB over the 1–100 MHz bandwidth, peaking at 112 dB at 1 MHz [see Fig. 10(b)]. The RX gain can be tuned from 30 to 110 dB at 21 MHz.

Fig. 11 summarizes the DLL measurement results. The 32 measured phases of the DLL demonstrate minimal phase errors of less than ±0.6° at 21 MHz, a performance deemed adequate for high-resolution spectroscopy [see Fig. 11(a)] [25]. Furthermore, it achieves an integrated rms jitter of 28.2/9.26 ps at 20/40 MHz, respectively [see Fig. 11(b)].

Fig. 12 shows the measured transient output waveforms of the PA and the DLL. The measured PA peak output waveform shows a single-ended, 9-V peak-to-peak swing, achieving a maximum drain efficiency of 49% with a 25-Ω load. The relative phase difference between the DLL and the PA can be programmed with a 5-bit selection code. The PA delivers a maximum peak output current of 860 mA on a 2-Ω load at 21 MHz (see Fig. 13). This digital PA contains 15 identical unit PA cells. The output current is tunable from 63 to 860 mA by turning on increasingly more unit PA cells. Because the PA output impedance is not constant with the changing number of activated unit PA cells, the PA output current will not be perfectly linear with the thermometer code (AM–AM distortion). This nonlinearity, however, is not an issue in our system operation, because for each excitation, a constant RF output current amplitude (a constant thermometer code) is always chosen from the 15 options.

Finally, Fig. 14 shows the RX gain and the TX output current over temperature. On the RX side, the LNA and VGA gains are the first-order temperature-insensitive due to their design [16]. On the TX side, since the Class-D PA operates by rapidly switching the output transistors between the fully on and fully off states as opposed to continuously conducting as in linear PA classes, temperature rise may be mitigated. In fact, the RX gain variations remain within 6 dB from 25 °C to 125 °C, and the PA output current degrades from 860 only to 740 mA across the same temperature range.

B. NMR Experiments

We now present NMR experiments with our system. Fig. 15 shows the ^{1}H FIDs of water at B_0 ~0.51 T and ~0.3 T (f_0 ~21.8 and ~12.8 MHz) to show the wideband operation of the CMOS chip. In either case, the B_0 field inhomogeneity is not compensated by shimming or motional averaging, and the resulting characteristic damping times of the FIDs, 82 and 3.6 ms, dominated by the effect of the B_0 field inhomogeneity are much shorter than T_2 due to pure spin–spin interactions (the characteristic time for such premature damping due to the B_0 field inhomogeneity is called T_2^*) [20]. The differing T_2^* values indicate that the 0.3-T magnet has a worse field inhomogeneity than the 0.51-T magnet.

Fig. 16(a) shows the ^{1}H NMR T_2 relaxometry measurement result, the envelops of spin echoes from the I and Q quadrature channels at the RX output, obtained with the CPMG sequence (B_0 ~0.51 T, water, single scan). A sample volume of 3.9 μL (length of the RF coil: 5 mm and inner diameter of the sample tube: 1 mm) is used. While the B_0 field inhomogeneity is still not compensated with shimming or motional averaging, the CPMG sequence overcomes the field inhomogeneity effect, with T_2 (as opposed to T_2^*) of ~0.61 s being measured, after removal of the baseline offset in the combined signal. Fig. 16(b) shows such T_2 measurements with only chip temperature, not sample temperature, varied from 25 °C to 125 °C with local heating with a heat gun, where each trace for a given temperature is a sum of 64 scans

TABLE I
COMPARISON WITH CMOS-BASED NMR SPECTROMETERS

Specifications	This work	[16] D. Krüger ESSCIRC'22	[11] S. Fan JSSC'22	[24] S. Hong VLSI'20	[6] K Lei Anal. Chem'20	[8] K. Lei ISSCC'16
System Performance						
Functionality	**NMR Relaxometry NMR Spectroscopy**	NMR Relaxometry NMR Spectroscopy	NMR Relaxometry	NMR Relaxometry	NMR Relaxometry NMR Spectroscopy	NMR Relaxometry
Magnet	**Permanent (0.3 T and 0.51 T)**	Permanent (0.51 T)	Permanent (0.52 T)	Permanent (0.5 T)	Permanent (0.51 T)	Permanent (0.46 T)
Shimming/ Gradient Control	**On-Chip**	On-Chip	Off-Chip	N/A	Off-Chip	N/A
Spectral Resolution	**0.07 ppm**	1 ppm	N/A	N/A	0.16 ppm	N/A
Multinuclear NMR	**Yes (^{1}H ^{19}F ^{2}H)**	No (**^{1}H**)	No (**^{1}H**)	No (**^{1}H**)	No (**^{1}H**)	No (**^{1}H**)
Circuit Performance						
Technology	**0.18μm CMOS**	0.18μm CMOS	0.18μm HV-CMOS SOI	0.18μm CMOS	0.18μm CMOS	0.18um CMOS
Frequency Range [MHz]	**1-100**	10-60	22.2	21	10-40	20
RX IRN [nV/√Hz]	**0.67*- 1.13**	0.78	0.63	0.95	0.82	1
RX Gain [dB]	**30-110**	30-100	85.2	65-125	34-100	87.6
RX Power Consumption [mW]	**47**	43	N/A	36	N/A	22.1
TX Maximum Pout [mW]	**740**	220	602	84	182	16
TX Efficiency [%]	**49**	39	N/A	N/A	N/A	31.6
Area [mm^2]	**5.6**	5	1.8	1.8	4	7.6

* Minimum RX IRN at 21 MHz

with 1 s between each scan to minimize noise. The 64-scan sum at 25 °C in Fig. 16(b) is smaller than 64 times the single-scan room temperature measurement of Fig. 16(a) due to the insufficient wait (1 s) for spins to thermally equilibrate between scans in the former. The measured T_2 values for the increasing temperatures in Fig. 16(b) are estimated to be 0.6, 0.6, 0.55, 0.62, and 0.6 s, where the baseline dc offsets are removed by phase cycling. Since only the chip temperature is varied, while the sample temperature is kept at the room temperature, the consistency between the T_2 value measured in Fig. 16(a) and the T_2 values measured in Fig. 16(b) confirms that the CMOS transceiver works reasonably well across the temperature range, with the amplitude drop with temperature in Fig. 16(b) arising from the temperature dependence of the entire transceiver.

Fig. 17 shows the effectiveness of shimming and motional averaging in reducing the B_0 field inhomogeneity. We use ^{1}H NMR spectroscopy to measure the NMR spectrum of ethanol. A sample volume of 0.15 μL (length of the RF coil: 1.2 mm and inner diameter of the tube: 0.4 mm) is used. In Fig. 17(a), the spectral resolution is 0.4 ppm, with neither shimming nor motional averaging. Upon enabling shimming, the spectral resolution improves to 0.24 ppm [see Fig. 17(b)]. Then, by combining shimming and motion averaging, the spectral resolution further improves to 0.07 ppm [see Fig. 17(c)]. Each spectrum of Fig. 17 is an average of 16 NMR spectroscopy scans to improve signal-to-noise ratio (SNR). Since the B_0 field fluctuation due to the drift of ambient temperature shifts NMR spectra in frequency, a software calibration scheme [7] is used to eliminate these shifts and align the 16 spectral scans before their averaging.

Fig. 18 explicitly shows the spectral shift due to the temperature drift over ca. 150 min. To begin with, note that each spectrum shown (whether black or red) is an average of 16 ^{1}H NMR spectroscopy scans of ethanol, with temperature drift during the 16 scans eliminated by the aforementioned software method. The black 16-scan average is the first set taken, and this identical black spectrum is repeatedly displayed across all 16 panels. On the other hand, the red spectrum in the nth panel ($n = 2, 3, \ldots, 16$) is the nth 16-scan average (the time gap between the starts of any two adjacent red 16-scan averages is 10 min).

The spectral shift over the ca. 150 min exceeds 2 ppm, which is much larger than the desired spectral resolution (<0.1 ppm).

Fig. 19 shows the ^{1}H, ^{19}F, and ^{2}H NMR spectroscopy results with shimming, motional averaging, and phase cycling enabled ($f_0 \approx$ 21.8, 20.5, and 3.3 MHz) for ethanol (16 scans), ethyl acetate (16 scans), methanol (16 scans), trifluoroethanol (64 scans), methyl nonafluorobutyl (64 scans), and deuterium oxide (16 scans). Not only chemical shifts but also J couplings are resolved, confirming the high-resolution spectroscopy capability of our system (e.g., a ^{1}H spectral resolution is 0.07 ppm, or 1.5 Hz for $f_0 \approx$ 21.8 MHz).

We also demonstrate NOE using our portable system (see Fig. 20). NOE involves the transfer of nuclear spin polarization between distinct nuclei in proximity, such as ^{1}H, ^{13}C, ^{15}N, and ^{19}F, accomplished through cross relaxation. In NMR, NOE can

be detected by the change in the integrated intensity of one NMR resonance when the other is saturated by an RF field. NOE provides an additional window to elucidate the structures of organic and biological molecules. In certain cases, NOE also improves NMR sensitivity [21], [22]. For example, NOE can enhance ^{19}F NMR signal with magnetization transfer from ^{1}H spins [21], [22].

Before testing ^{1}H–^{19}F NOE [see Fig. 20(c)], we verified the capability of saturating ^{1}H and ^{19}F signals [see Fig. 20(a) and (b)]. In all three panels of Fig. 20, T_s is the total duration of applying saturation RF pulses, and *tau* is the delay between the last saturation pulse and the start of the CPMG sequence. *tau* is varied from 0.1 to 4 s, and in reality, there is an extra 0.1-s delay due to switching, making $T = tau + 0.1$ s (T is the horizontal axis for each of the three graphs in Fig. 20). In Fig. 20(a), a train of $\pi/2$ pulses saturates ^{1}H spins, and a ^{1}H spin echo readout with CPMG sequence follows (each data point in the graph is acquired from the first spin echo peak with 64 scans). For a larger *tau* or for a larger T, the ^{1}H spin echo readout has a larger amplitude, because the saturation is increasingly released with the larger T. This confirms the ability of our system to saturate ^{1}H spins. Similar saturation measurements are done for ^{19}F spins [see Fig. 20(b)]. Fig. 20(c) shows NOE with saturated ^{1}H spins and CPMG read ^{19}F spins. Concretely, for a larger T after the ^{1}H spin saturation, the ^{19}F spin echo amplitude is decreased, because a longer T leads to a decreased ^{1}H spin saturation, thus less NOE for the ^{19}F spins [blue circles, Fig. 20(c)]. The NOE enhancement of the ^{19}F NMR signal is as large as 18% [note that red squares, Fig. 20(c), are for the first ^{19}F spin echo amplitude without NOE].

C. Comparison With Other Works

Table I summarizes the performance of the CMOS-based portable NMR spectrometers [6], [8], [11], [16], [24] in juxtaposition with our work. The wideband frequency range of our system enables NMR work with multinuclear NMR experiments. In addition, we conducted an NOE experiment. Circuit details are also compared in Table I.

V. Conclusion

We presented a CMOS-based small NMR system capable of multinuclear NMR spectroscopy (with ^{1}H, ^{19}F, and ^{2}H NMR spectroscopy experiments as demonstrational examples) and heteronuclear NOE (with ^{1}H–^{19}F NOE as a demonstrational example with an 18% signal enhancement for the ^{19}F NMR signal) with its wideband operation. Our system reaches an NMR spectral resolution down to 0.07 ppm. This miniaturized multinuclear NMR system can enhance the capability for online molecular fingerprinting. In addition, we demonstrated NMR relaxometry under different temperatures, showing the temperature resilience of the system design. This multimodal, multinuclear miniaturized NMR system is enabled by the CMOS RF transceiver IC incorporating the wideband DLL and the digital power amplifier.

References

[1] K. Wüthrich, "NMR with proteins and nucleic acids," *Europhys. News*, vol. 17, no. 1, pp. 11–13, 1986.

[2] J. D. Roberts, *Nuclear Magnetic Resonance: Applications to Organic Chemistry*. New York, NY, USA: McGraw-Hill, 1959.

[3] K. Wüthrich, "The way to NMR structures of proteins," *Nature Struct. Biol.*, vol. 8, no. 11, pp. 923–925, 2001.

[4] Y. Liu, N. Sun, H. Lee, R. Weissleder, and D. Ham, "CMOS mini nuclear magnetic resonance system and its application for biomolecular sensing," in *IEEE Int. Solid-State Circuits Conf. (ISSCC) Dig. Tech. Papers*, Feb. 2008, pp. 140–141.

[5] N. Sun, T.-J. Yoon, H. Lee, W. Andress, R. Weissleder, and D. Ham, "Palm NMR and 1-chip NMR," *IEEE J. Solid-State Circuits*, vol. 46, no. 1, pp. 342–352, Jan. 2011.

[6] K.-M. Lei et al., "Portable NMR with parallelism," *Anal. Chem.*, vol. 92, no. 2, pp. 2112–2120, Jan. 2020.

[7] D. Ha, J. Paulsen, N. Sun, Y.-Q. Song, and D. Ham, "Scalable NMR spectroscopy with semiconductor chips," *Proc. Nat. Acad. Sci. USA*, vol. 111, no. 33, pp. 11955–11960, Aug. 2014.

[8] K.-M. Lei, H. Heidari, P.-I. Mak, M.-K. Law, F. Maloberti, and R. P. Martins, "28.1 A handheld 50 pM-sensitivity micro-NMR CMOS platform with B-field stabilization for multi-type biological/chemical assays," in *IEEE Int. Solid-State Circuits Conf. (ISSCC) Dig. Tech. Papers*, Jan. 2016, pp. 474–475.

[9] S. Hong and N. Sun, "Portable CMOS NMR system with 50-kHz IF, 10-μs dead time, and frequency tracking," *IEEE Trans. Circuits Syst. I, Reg. Papers*, vol. 68, no. 11, pp. 4576–4588, Nov. 2021.

[10] H. Bürkle, T. Klotz, R. Krapf, and J. Anders, "A 0.1 MHz to 200 MHz high-voltage CMOS transceiver for portable NMR systems with a maximum output current of 2.0 app," in *Proc. IEEE 47th Eur. Solid State Circuits Conf. (ESSCIRC)*, Sep. 2021, pp. 327–330.

[11] S. Fan, Q. Zhou, K.-M. Lei, P.-I. Mak, and R. P. Martins, "A miniaturized 3-D-MRI scanner featuring an HV-SOI ASIC and achieving a $10 \times 8 \times 8$ mm^3 field of view," *IEEE J. Solid-State Circuits*, vol. 58, no. 7, pp. 2028–2039, Jul. 2023.

[12] D. Krüger et al., "A portable CMOS-based spin resonance system for high-resolution spectroscopy and imaging," *IEEE J. Solid-State Circuits*, vol. 58, no. 7, pp. 1838–1849, Jul. 2023.

[13] J. Anders and A. H. Velders, *Microcoils for Broadband Multinuclei Detection*. Hoboken, NJ, USA: Wiley, 2018, ch. 1, pp. 265–296.

[14] J. Anders, F. Dreyer, D. Krüger, I. Schwartz, M. B. Plenio, and F. Jelezko, "Progress in miniaturization and low-field nuclear magnetic resonance," *J. Magn. Reson.*, vol. 322, Jan. 2021, Art. no. 106860.

[15] F. Dreyer, D. Krüger, S. Baas, A. Velders, and J. Anders, "A 5–780-MHz transceiver ASIC for multinuclear NMR spectroscopy in 0.13-μ m BiCMOS," *IEEE Trans. Circuits Syst. I, Reg. Papers*, vol. 70, no. 9, pp. 3484–3496, Sep. 2023.

[16] D. Krüger et al., "A portable CMOS-based MRI system with $67\times67\times83$ μm^3 image resolution," in *Proc. IEEE 48th Eur. Solid State Circuits Conf. (ESSCIRC)*, Milan, Italy, Sep. 2022, pp. 225–228.

[17] A. Zhang et al., "A wideband CMOS NMR spectrometer for multinuclear molecular fingerprinting," in *Proc. IEEE Symp. VLSI Technol. Circuits (VLSI Technol. Circuits)*, Jun. 2023, pp. 1–2.

[18] A. Zhang and M. S. Chen, "A sub-harmonic switching digital power amplifier with hybrid class-G operation for enhancing power back-off efficiency," in *Proc. IEEE Symp. VLSI Circuits*, Honolulu, HI, USA, Jun. 2018, pp. 213–214.

[19] A. Zhang and M. S. Chen, "A subharmonic switching digital power amplifier for power back-off efficiency enhancement," *IEEE J. Solid-State Circuits*, vol. 54, no. 4, pp. 1017–1028, Apr. 2019.

[20] H. Y. Carr and E. M. Purcell, "Effects of diffusion on free precession in nuclear magnetic resonance experiments," *Phys. Rev.*, vol. 94, no. 3, pp. 630–638, May 1954.

[21] I. Kuprov and P. J. Hore, "Chemically amplified 19F–1H nuclear overhauser effects," *J. Magn. Reson.*, vol. 168, no. 1, pp. 1–7, May 2004.

[22] B. Chaubey, A. Dey, A. Banerjee, N. Chandrakumar, and S. Pal, "As-sessment of the role of 2,2,2-trifluoroethanol solvent dynamics in inducing conformational transitions in melittin: An approach with solvent ^{19}F low-field NMR relaxation and overhauser dynamic nuclear polarization studies," *J. Phys. Chem. B*, vol. 124, no. 28, pp. 5993–6003, 2020.

[23] B. Krems, P. Bachert, H. J. Zabel, and W. J. Lorenz, "^{19}F-^{1}H nuclear overhauser effect and proton decoupling of 5-fluorouracil and α-fluoro-β-alanine," *J. Magn. Reson., B*, vol. 108, no. 2, pp. 155–164, Aug. 1995.

[24] S. Hong and N. Sun, "A portable NMR system with 50-kHz IF, 10-us dead time, and frequency tracking," in *Proc. IEEE Symp. VLSI Circuits*, Honolulu, HI, USA, Jun. 2020, pp. 1–2.
[25] J. Anders, P. SanGiorgio, and G. Boero, "A quadrature receiver for μNMR applications in 0.13 μm CMOS," in *Proc. ESSCIRC*, Seville, Spain, Sep. 2010, pp. 394–397.
[26] J. Anders, P. SanGiorgio, and G. Boero, "An integrated CMOS receiver chip for NMR-applications," in *Proc. IEEE Custom Integr. Circuits Conf.*, San Jose, CA, USA, Sep. 2009, pp. 471–474.
[27] S. Meiboom and D. Gill, "Modified spin-echo method for measuring nuclear relaxation times," *Rev. Sci. Instrum.*, vol. 29, pp. 688–691, 1958.

Aoyang Zhang (Member, IEEE) received the B.S. degree (Hons.) from Zhejiang University, Hangzhou, China, in 2014, and the Ph.D. degree from the University of Southern California, Los Angeles, CA, USA, in 2020, all in electrical engineering.

From 2021 to 2023, he was a Post-Doctoral Fellow with Harvard University, Cambridge, MA, USA. He is currently an Assistant Professor with Tsinghua University, Beijing, China. His research interests include energy efficient reconfigurable RF/mixed-signal integrated circuits design for communications and sensing, new computing platforms with analog and mixed-signal circuits, and hardware security circuits.

Dr. Zhang was a recipient of the 2021 USC Best Dissertation Award in Electrical Engineering, the 2020–2021 IEEE Solid-State Circuits Society (SSCS) Predoctoral Achievement Award, the 2020–2021 Ming Hsieh Institute Scholar, the IEEE SSCS Student Travel Grant Award (STGA) in 2018, the Best Bachelor Thesis Award in 2014, and the First Prize of Chinese National Mathematical Competition in 2010.

Daniel Krüger (Member, IEEE) received the B.S. and M.S. degrees in electrical engineering from the University of Stuttgart, Stuttgart, Germany, in 2016 and 2018, respectively, where he is currently pursuing the Ph.D. degree from the Institute of Smart Sensors.

He is a Research Fellow with the Donhee Ham Laboratory, Harvard University, Cambridge, MA, USA. His research interests include mixed-signal integrated circuits (ICs) for nuclear magnetic resonance (NMR), electron spin resonance (ESR), and biomedical applications.

Behdad Aghelnejad was a Post-Doctoral Research Fellow with Harvard University, Cambridge, MA, USA, where he helped to develop low-field NMR and MRI handheld devices. Before that, he has gained experience working on MRI-, NMR-, and EPR-related technologies at École Normale Supérieure (ENS), Paris, France, and Martin Luther University Halle-Wittenberg, Halle, Germany. He started as part of the Oxford Instruments Magnetic Resonance Technology Team as a Senior Development Physicist, where he was recently promoted to the role of the Principal Technologist.

Guang Yang received the Ph.D. degree from Victoria University of Wellington, Wellington, New Zealand, in 2022, with a focus on constructing a scalable MRI console with multichannel transceivers for inhomogeneous fields.

He is currently a Post-Doctoral Researcher at Harvard University, Cambridge, MA, USA, under the supervision of Prof. Donhee Ham. He focuses on developing a miniature magnetic field sensor subsystem based on the NMR ASICs. This subsystem aims to monitor magnetic field imperfections during MRI scans, with the goal of enhancing overall image quality.

Henry Hinton (Member, IEEE) received the B.S. degree in biomolecular engineering from the University of California at Santa Cruz, Santa Cruz, CA, USA, in 2018, and the M.S. and Ph.D. degrees in electrical engineering from Harvard University, Cambridge, MA, USA, in 2021 and 2023, respectively.

He currently works on brain–computer interfaces at Axoft, Cambridge, as the Scientist. His research interests include integrated circuit design for biological, optoelectronic, electrochemical interfaces, and devices using emerging materials.

Yi-Qiao Song received the B.S. degree from Peking University, Beijing, China, in 1985, and the Ph.D. degree from Northwestern University, Evanston, IL, USA, in 1991.

He was a Miller Research Fellow with the University of California at Berkeley, Berkeley, CA, USA, where he studied hyperpolarized gases. From 1997 to 2020, he was with Schlumberger-Doll Research, Cambridge, MA, USA, to develop NMR/MRI for porous media and well logging. He is currently a Senior Scientist with Harvard University, Cambridge, MA, USA, and a Research Staff with Massachusetts General Hospital, Boston, MA, USA. He has published over 190 scientific articles and holds more than 60 patents.

Dr. Song is a fellow of American Physical Society and International Society of Magnetic Resonance, an Associate Editor of the *Frontier of Physics* and *Petroleum Sciences*, and a member of the editorial boards at the *Journal of Magnetic Resonance*, *Magnetic Resonance Letters*, and *Chinese Journal of Magnetic Resonance*. He is the Chair of the Magnetic Resonance in Porous Media Division of Groupement Ampere.

Donhee Ham (Fellow, IEEE) is currently a Gordon McKay Professor of applied physics and electrical engineering with Harvard University, Cambridge, MA, USA, where he has been a Faculty Member, since 2002. He is a Samsung Fellow. His current research interests include semiconductor-bio interfaces for neuroscience, machine intelligence, and biological data archiving; scalable nuclear magnetic resonance (NMR); integrated circuits; neuromorphic and in-sensor computing; and beyond CMOS electronics.